Pergamon

International Journal of Plasticity, Vol. 14, No. 8, pp. 733–754, 1998
© 1998 Elsevier Science Ltd
Printed in Great Britain. All rights reserved
0749-6419/98 $—see front matter

PII: S0749-6419(98)00020-5

THE GROWTH OF SHEAR BANDS IN COMPOSITE MICROSTRUCTURES

Min Zhou*

The George W. Woodruff School of Mechanical Engineering, Georgia Institute of Technology, Atlanta, GA 30332-0405, U.S.A.

(*Received in final revised form* 18 *August* 1997)

Abstract—Shear band formation in materials with inhomogeneous and composite microstructures is influenced by factors that usually do not come into play in monolithic materials. Experiments and calculations have shown that inhomogeneities in material properties enhance the localization of deformation. This investigation concerns the propagation of shear bands in a two-phase tungsten composite under the conditions of nominally pure shear deformation. Finite element calculations are carried out to delineate the effects of different grain–matrix morphologies. In the numerical models, the initiation of shear bands is triggered by a notch, simulating the effect of defects such as microcracks and microvoids in materials. Calculations demonstrate that phase morphology, particle size and the relative location of initiation site have significant influences on the development of localized deformation. The work and energy evolutions are tracked for each constituent phase in the microstructures. In addition, the exchange of thermal energy through heat flow between the phases is analyzed. The results show that a strong correlation exists between the course of shear band propagation and the thermomechanical coupling between microscopic phases. © 1998 Elsevier Science Ltd. All rights reserved

Key words: Shear localization, shear band propagation, tungsten composite, tungsten heavy alloy, inhomogeneous materials.

I. INTRODUCTION

Shear band formation in materials with composite and inhomogeneous microstructures is influenced by factors that usually do not come into play in monolithic materials. The inherent heterogeneities in material properties promote nonuniform deformation in the microscopic constituents, thus enhancing the tendency for localization through coupled thermomechanical interactions, Zhou *et al.* (1994). For example, in the tungsten composites or tungsten heavy alloys analyzed by Lankford *et al.* (1991), Magness (1994), Andrews *et al.* (1992), Weerasooriya *et al.* (1992) Yadav and Ramesh (1995) and Zhou *et al.* (1997) nearly spherical tungsten particles are surrounded by a ductile matrix which is an alloy of nickel, tungsten and iron or nickel and cobalt. The particles have higher flow stresses, a higher density, a lower rate of strain hardening, a higher strain rate sensitivity, a higher thermal conductivity, and a lower specific heat. The matrix has relatively lower flow stresses, a lower density, a higher rate of strain hardening, a lower strain rate sensitivity,

*Corresponding author. Fax: 001 404 894 0186; e-mail: min.zhou@me.gatech.edu

a lower thermal conductivity, and a higher specific heat. The different combinations of thermomechanical properties constitute an environment for thermomechanical coupling between the phases and provide a driving force for nonuniform deformation. The lower flow stresses of the matrix allow it to deform at higher rates than the particles initially, therefore generating heat through plastic dissipation. The higher thermal conductivity of the particles allows them to absorb heat from the matrix, causing their temperatures to increase and their flow stress to drop. This process enables the hard particles to deform more than a monolithic material with the properties of the particles would under the same loading conditions. On the other hand, the higher flow stresses of the particles allow the matrix to deform more than a monolithic matrix material would under the same conditions. This thermomechanical coupling due to inhomogeneous material properties causes composite materials to be more susceptible to shear localization than its individual constituents if they are deformed separately.

In addition to expediting the localization of deformation, the presence of hard and soft microscopic phases can also impede the propagation of shear bands. By design, hard particles are intended to be reinforcement against deformation and failure. The presence of hard particles or grains can act as "road blocks" for growing shear bands. Such an effect may be significant if they are located along the likely paths of propagating shear bands, requiring more external mechanical work to be supplied for further deformation. The driving force for nonuniform deformation and the strengthening effect of hard particles represent competing influences on shear localization in an inhomogeneous material. The former contributes to expedite localization and the latter acts to impede the growth of shear bands.

This paper analyzes the initiation and growth of shear bands in a two-phase microstructure similar to those of the materials studied by Magness (1994), Andrews *et al.* (1992), Weerasooriya *et al.* (1992) and Zhou and Clifton (1997). Finite element calculations are carried out using microstructures with the actual phase morphologies of a tungsten heavy alloy and several assumed particle–matrix distributions involving different particle sizes. In addition to accounting for microstructure, the numerical model also simulates the effect of microflaws, such as voids, microcracks, and interface debonding, by considering a small notch in the material. This notch serves as a trigger for the initiation and propagation of shear localization. The width of the notch is small compared with the width of the shear bands and the grain size. In addition, the same notch geometry is used for all the microstructures analyzed. Under such conditions, it is assumed that qualitative features of shear band initiation from microflaws can be demonstrated. However, rather than focusing on how flaws trigger the onset of shear localization, the analysis reported here mainly concerns the interaction between shear bands and microscopic phases after the bands initiate. The objective is to characterize the influence of different microstructural phase morphologies in composite materials on the growth of shear bands.

II. FRAMEWORK OF ANALYSIS

II.1. *Momentum and energy balance*

A convected coordinate, Lagrangian formulation of the field equations is used as, for example, in Lemonds and Needleman (1986), Needleman (1989) and Needleman and Tvergaard (1991). The independent variables are the particle coordinates, ξ^i, in the initial

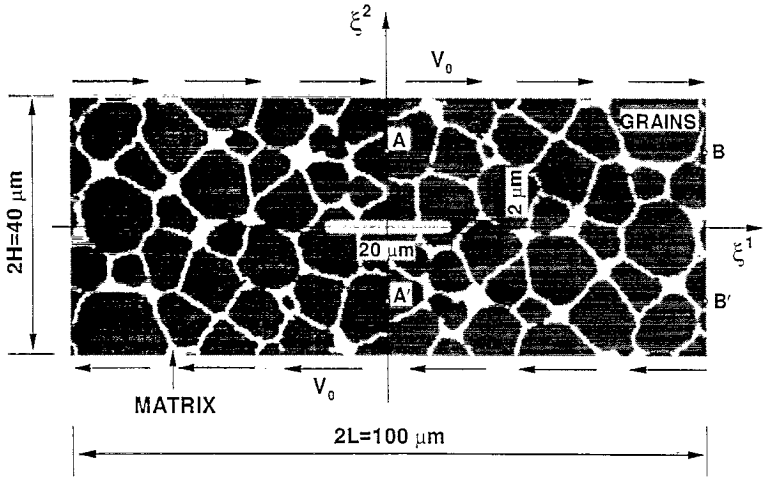

Fig. 1. Material block with random phase distribution analyzed; the coordinate system and velocity boundary conditions are also illustrated. This microstructure has a grain volume fraction of approximately 85% and a matrix volume fraction of 15%.

stress free configuration (Fig. 1) and time, t. A material point initially at $\mathbf{x}$ in the reference configuration assumes a position $\bar{\mathbf{x}}$ in the current configuration. The displacement vector $\mathbf{u}$ and the deformation gradient tensor are defined by

$$\mathbf{u} = \bar{\mathbf{x}} - \mathbf{x}, \mathbf{F} = \frac{\partial \bar{\mathbf{x}}}{\partial \mathbf{x}}. \tag{1}$$

The dynamic deformation of materials is a coupled thermomechanical process. The mechanical part is governed by the balanced of momentum and the thermal part is governed by the balance of energy (heat equation). These two systems of equations are written as the principle of virtual work

$$\int_V \boldsymbol{\tau} : \delta \mathbf{D} \mathrm{d}V = \int_S \mathbf{f} \cdot \delta \dot{\mathbf{u}} \mathrm{d}S - \int_V \rho \frac{\partial^2 \mathbf{u}}{\partial t^2} \cdot \delta \dot{\mathbf{u}} \mathrm{d}V, \tag{2}$$

and the variational heat equation

$$\begin{aligned} \int_V \rho c_p \dot{T} \delta T \mathrm{d}V = & \int_V \chi \boldsymbol{\tau} : \mathbf{D}^p \delta T \mathrm{d}V + \int_S K\left(\mathbf{F}^{-1} \cdot \mathbf{F}^{-T} \cdot \frac{\partial T}{\partial x}\right) \cdot \mathbf{n} \delta T \mathrm{d}S \\ & - \int_V k\left(\mathbf{F}^{-1} \cdot \mathbf{F}^{-T} \cdot \frac{\partial T}{\partial x}\right) \cdot \frac{\partial \delta T}{\partial x} \mathrm{d}V, \end{aligned} \tag{3}$$

where V, S and ρ are the volume, surface and mass density, respectively, of the body in the reference configuration. $\boldsymbol{\tau} = J\boldsymbol{\sigma} = \det|\mathbf{F}|\boldsymbol{\sigma}$ is the Kirchhoff stress, with $\boldsymbol{\sigma}$ the Cauchy stress. $\mathbf{f}$ is the traction on a surface with normal $\mathbf{n}$ in the reference configuration, $\mathbf{D}$ denotes the rate of deformation tensor, T is temperature, χ denotes the fraction of plastic work converted to heat, $\mathbf{D}^p$ is the plastic part of $\mathbf{D}$, c_p is specific heat, k is thermal conductivity, $(\dot{})$

denotes $\partial/\partial t$, $()^{-1}$ and $()^{-T}$ denote, respectively, inverse and inverse transpose. The dyadic product $\mathbf{A} : \mathbf{B}$ is $A^{ij}B_{ji}$. δT, $\delta\mathbf{D}$ and $\delta\dot{\mathbf{u}}$ denote admissible variations in temperature, rate of deformation and particle velocity, respectively. These two systems of equations are coupled through the heat generation term in (3).

II.2. *Constitutive relation*

Under the conditions of small elastic strains, assuming that the thermoelastic coupling is negligible and ignoring any temperature dependence of the elastic moduli, one can write the incremental stress–deformation rate relation as

$$\hat{\boldsymbol{\tau}} = \mathbf{L} : [\mathbf{D} - \mathbf{D}^p - \alpha\dot{T}\mathbf{I}], \tag{4}$$

where $\hat{\boldsymbol{\tau}}$ is the Jaumann rate of Kirchhoff stress, $\mathbf{L}$ is the tensor of elastic moduli, α is the coefficient of thermal expansion, $\mathbf{I}$ is the second order identity tensor. For isotropic, thermoelastic response,

$$\mathbf{L} = \frac{E}{1+\nu}\left[\mathbf{I}' + \frac{\nu}{1-2\nu}\mathbf{I}\otimes\mathbf{I}\right]. \tag{5}$$

Here, $\mathbf{I}'$ is the fourth order identity tensor, E is Young's modulus, ν is Poisson's ratio and $\mathbf{A}\otimes\mathbf{B}$ denotes the tensor product.

For an isotropically hardening, viscoplastic solid, $\mathbf{D}^p$ is given by

$$\mathbf{D}^p = \frac{3\dot{\bar{\epsilon}}}{2\bar{\sigma}}\boldsymbol{\tau}', \tag{6}$$

with $\dot{\bar{\epsilon}}$ being the equivalent plastic strain rate and

$$\boldsymbol{\tau}' = \boldsymbol{\tau} - \frac{1}{3}(\boldsymbol{\tau} : \mathbf{I})\mathbf{I}, \qquad \bar{\sigma}^2 = \frac{3}{2}\boldsymbol{\tau}' : \boldsymbol{\tau}'. \tag{7}$$

The thermoviscoplastic response of each of the constituent materials in the composite microstructures is characterized by the following thermoviscoplastic relations

$$\left.\begin{aligned}
\dot{\bar{\epsilon}} &= \frac{\dot{\epsilon}_1\dot{\epsilon}_2}{\dot{\epsilon}_1+\dot{\epsilon}_2},\\
\dot{\epsilon}_1 &= \dot{\epsilon}_0\left[\frac{\bar{\sigma}}{g(\bar{\epsilon},T)}\right]^m,\\
\dot{\epsilon}_2 &= \dot{\epsilon}_m\exp\left[-\frac{ag(\bar{\epsilon},T)}{\sigma}\right],\\
g(\bar{\epsilon},T) &= \sigma_0(1+\bar{\epsilon}/\epsilon_0)^N\left\{1-\beta\left(-\frac{T-T_0}{T_d}\right)\right\}s(T),\\
s(T) &= \begin{cases} 1, & T\le T_c,\\ \left[1-\left(\frac{T-T_c}{T_m-T_c}\right)^2\right], & T_c\le T\le T_m. \end{cases}
\end{aligned}\right\} \tag{8}$$

In the above equations, $\bar{\epsilon} = \int_0^t \dot{\bar{\epsilon}} dt$ is the equivalent plastic strain, $\dot{\epsilon}_0$ is a reference strain rate, $\bar{\sigma}$ is the Mises equivalent stress, m and a are rate sensitivity parameters, respectively, for strain rates below $10^{-3}s^{-1}$ and above $5 \times 10^4 s^{-1}$, σ_0 is a reference stress, ϵ_0 is a reference strain, N is a strain hardening exponent, T_0 is a reference temperature, and β and T_d are thermal softening parameters. Function $g(\bar{\epsilon}, T)$ represents the stress–strain relation at a quasi-static strain rate of $\dot{\epsilon}_0$ and at temperature T. At $T = T_0$, $g(\bar{\epsilon}, T_0) = \sigma_0(1 + \bar{\epsilon}/\epsilon_0)^N$. Function $s(T)$ is introduced to model higher rates of thermal softening at higher temperatures. T_c is a threshold temperature for $s(T)$ to become active, and T_m is the melting temperature. The relations in (8) account for strain hardening, thermal softening, and strain rate sensitivity. This particular form involving two strain rate functions ($\dot{\epsilon}_1$ and $\dot{\epsilon}_2$) is chosen based on experimental measurement of the shear stress–strain relations over the strain rate range of 10^{-3} to 10^5 s^{-1}. Specifically, $\dot{\epsilon}_1$ describes the strain hardening behavior in the strain rate range of 10^{-1} to $10^3 s^{-1}$ and $\dot{\epsilon}_2$ models the enhanced strain hardening behavior between 10^3 and 10^6 s^{-1}. The functional form used provides a smooth transition of behavior between these two strain rate regions. Model parameters for the constituent phases are determined using experimental data reported in Zhou *et al.* (1997) and are listed in Table 1.

III. FINITE ELEMENT METHOD

Finite element discretization is based on triangular elements arranged in "crossed triangle" quadrilaterals. Displacements and temperature are taken to vary linearly over the triangular elements. When the finite element approximations of the displacement and temperature fields are substituted into the momentum balance (3) and the energy balance (4) relations, the resulting equations take the form,

$$\mathbf{M}\frac{\partial^2 \mathbf{U}}{\partial t^2} = \mathbf{R} \tag{9}$$

Table 1. Material model parameters

Parameter	Grains	Matrix
$\dot{\epsilon}_0$	1.0×10^{-4} s^{-1}	1.0×10^{-4} s^{-1}
m	50	17
σ_0	730 MPa	100 MPa
$\dot{\epsilon}_m$	8.0×10^{8} s^{-1}	8.0×10^{10} s^{-1}
a	21	1
ϵ_0	1.83×10^{-5}	3.92×10^{-4}
N	0.05	0.20
β	0.85	0.85
T_0	293 K	293 K
T_d	600 K	600 K
k	160 W(m.K)$^{-1}$	100 W(m.K)$^{-1}$
c_p	138 J(kg.K)$^{-1}$	382 J(kg.K)$^{-1}$
χ	0.9	0.9
ρ	19 300 kgm^{-3}	9200 kgm^{-3}
E	4.00×10^5 MPa	2.55×10^5 MPa
ν	0.29	0.29
α	5.3×10^{-6} K^{-1}	1.5×10^{-5} K^{-1}

and

$$\mathbf{C}\frac{\partial \mathbf{T}}{\partial t} = -\mathbf{K}\mathbf{T} + \mathbf{H}, \tag{10}$$

where $\mathbf{U}$ is the vector of nodal displacements, $\mathbf{T}$ is the vector of nodal temperatures, $\mathbf{M}$, $\mathbf{C}$ and $\mathbf{K}$ are, respectively, the mass, the heat capacitance and the heat conductance matrices, and $\mathbf{R}$ and $\mathbf{H}$ are the mechanical and thermal force vectors.

A lumped mass matrix is used in (9), for reasons of efficiency and accuracy, Krieg and Key (1973). Additionally, a lumped heat capacitance matrix is used in (10). In order to verify the accuracy of the integration of (10) with a lumped capacitance matrix, numerical results for a purely thermal problem involving non-uniform heat sources distributed on a rectangular area were compared with an analytical solution and good agreement was found.

Equations (9) and (10) are decoupled and solved using a staggered scheme consisting of alternating isothermally mechanical and pure thermal processes. For each time step, the displacements and velocities are first obtained by integrating the equations of motion (9) using an explicit integration method, the Newmark β-method, with $\beta = 0$ and $\gamma = 0.5$, Belytschko *et al.* (1976). After the deformation field is obtained, $\boldsymbol{\tau} : \mathbf{D}^p$, is calculated and its contribution to the thermal force $\mathbf{H}$ is determined. The temperature rates and temperatures are then obtained from (10). The rate tangent modulus expansion of Peirce *et al.* (1984) is used to update the stress tensor $\boldsymbol{\tau}$. Time increments used in the calculation are small fractions of the time it takes for the longitudinal stress wave to traverse the smallest finite element in the more stiff material (the grains) in the microstructure. The increment for each time step is adjusted using an empirical formula limiting the maximum changes in equivalent stress, equivalent plastic strain and temperature during the time step.

IV. PROBLEM ANALYZED

The problem analyzed is illustrated in Fig. 1. A block of material is assumed to contain a notch 20 μm in length and 2 μm in width centered in the middle. This notch is a trigger for localization, simulating the effect of a microcrack or a void in the material. Since shear bands are expected to have widths of the order of 10–15 μm, the dimensions of the specimen is chosen to be 100 μm×4 μm, sufficient for the analysis of shear band development in such a microstructure. The mesh used has approximately 100×40 quadrilaterals or 100×40×4 triangular elements. The smallest element is at the notch tip where the deformation is expected to be most intense. This element has a size of approximately 0.35 μm.

The material is subjected to nominally pure shear deformation. This overall deformation is specified by the velocity histories at the top ($\xi^2 = H$) and the bottom ($\xi^2 = -H$) surfaces. These velocity histories are

$$\left.\begin{aligned} \dot{u}^1(\xi^1, H, t) = -\dot{u}^1(\xi^1, -H, t) &= \begin{cases} V_0 t/t_r, & 0 \le t \le t_r, \\ V_0, & t \ge t_r, \end{cases} \\ \dot{u}^2(\xi^1, H, t) = \dot{u}^2(\xi^1, -H, t) &= 0, \quad t \ge 0; \end{aligned}\right\} \tag{11}$$

where t_r is the risetime over which the boundary velocity is increased from 0 to V_0. In the calculations, this risetime is chosen to be 0.1 μs. After this time, the applied boundary velocity is V_0 and the specimen is sheared at a constant, nominal rate of V_0/H.

The material block shown is assumed to be one unit cell of a thin foil extending infinitely and repeating itself periodically in the $+\xi^1$ and $-\xi^1$ directions. The periodicity allows the following periodic boundary conditions to be applied at the left ($\xi^1 = -L$) and right ($\xi^1 = L$) boundaries,

$$\left.\begin{aligned} \mathbf{u}(-L, \xi^2, t) &= \mathbf{u}(L, \xi^2, t), \\ T(-L, \xi^2, t) &= T(L, \xi^2, t). \end{aligned}\right\}; \quad -H \le \xi^2 \le H. \tag{12}$$

In addition to the periodicity and in order to reduce the size of the numerical model, the material block is chosen such that phase distributions in the left half ($\xi^1 \le 0$) and the right half ($\xi^1 \ge 0$) are antisymmetric to each other with respect to the origin $(\xi^1, \xi^2) = (0, 0)$. This antisymmetry makes it possible to use only one half (e.g. the right half where $\xi^1 \ge 0$) of the material block in the numerical calculations. To achieve this reduction, the following antisymmetric boundary conditions are applied

$$\left.\begin{aligned} \mathbf{u}(0, \xi^2, t) &= -\mathbf{u}0, -\xi^2, t), \\ T(0, \xi^2, t) &= T(0, -\xi^2, t), \end{aligned}\right\}; \quad -H \le \xi^2 \le H. \tag{13}$$

The lumped mass and capacitance matrices $\mathbf{M}$ and $\mathbf{C}$ in eqns (9) and (10) allow easy implementation of the periodic boundary conditions (12) and the antisymmetric boundary conditions (13). Specifically, for nodes A and A' on $\xi^1 = 0$ that satisfy $(\xi^2)_A = -(\xi^2)_{A'}$

$$\frac{\partial^2 \mathbf{U}}{\partial t^2}\Big|_A = -\frac{\partial^2 \mathbf{U}}{\partial t^2}\Big|_{A'} = \frac{(\mathbf{R})_A - (\mathbf{R})_{A'}}{(\mathbf{M})_A + (\mathbf{M})_{A'}}, \tag{14}$$

and

$$\dot{\mathbf{T}}\,|_A = \dot{\mathbf{T}}\,|_{A'} = \frac{(-\mathbf{KT} + \mathbf{H})_A + (-\mathbf{KT} + \mathbf{H})_{A'}}{(\mathbf{C})_A + (\mathbf{C})_{A'}}, \tag{15}$$

where $(\ )_A$ and $(\ )_{A'}$ denote the components of the matrices associated with the two nodes, respectively. For example, $(\mathbf{M})_A$ and $(\mathbf{M})_{A'}$, are the nodal masses for A and A', respectively, and $(\mathbf{C})_A$ and $(\mathbf{C})_{A'}$ are the corresponding nodal capacitances for these two nodes. The boundary conditions for nodes B and B' on $\xi^1 = L$ that satisfy $(\xi^2)_B = -(\xi^2)_{B'}$ are implemented in the same manner.

The thermal boundary conditions at the upper and lower surfaces are such that no heat exchange is allowed between the specimen and its surroundings. These conditions can be written as

$$\frac{\partial T}{\partial \mathbf{x}} \cdot \mathbf{n} = 0, \; -L \le \xi^1 \le L, \; \xi^2 + \pm H. \tag{16}$$

Initially at $t = 0$, the specimen is at rest and stress-free. The initial temperature is at T_0.

The random phase distribution in Fig. 1 is from the actual microstructure of a tungsten composite used in the study of Zhou and Clifton (1997). This microstructure has a grain

volume fraction of approximately 85% and a matrix volume fraction of approximately 15%. In order to delineate the effect of different microstructural morphologies on the initiation and propagation of shear bands, four other microstructures are also used in the numerical analysis. These four microstructures consist of regular arrays of circular (cylindrical in 3D) particles in a matrix and are shown in Fig. 2. The volume fraction for the particles is 75.4% and the volume fraction for the matrix is 24.6% in these four microstructures. Microstructures (a) and (b) have the same particle diameter of 10 μm. The only difference between these two cases is the relative locations of the notch and the particles. In Fig. 2(a), the notch is located between two rows of particles, providing a relatively soft path for the initiation and growth of a shear band from the notch tip. In Fig. 2(b), the notch is at the center of a row of particles, the higher flow stresses of the particle material pose a stronger resistance to deformation directly in front of a potential shear band initiating from the notch tip. The notch-particle arrangements in Fig. 2(c) and (d) are similar to that in Fig. 2(b). However, the particle size is successively reduced to 5 μm in Fig. 2(c) and 2.5 μm Fig. 2(d), respectively. The different particle sizes in

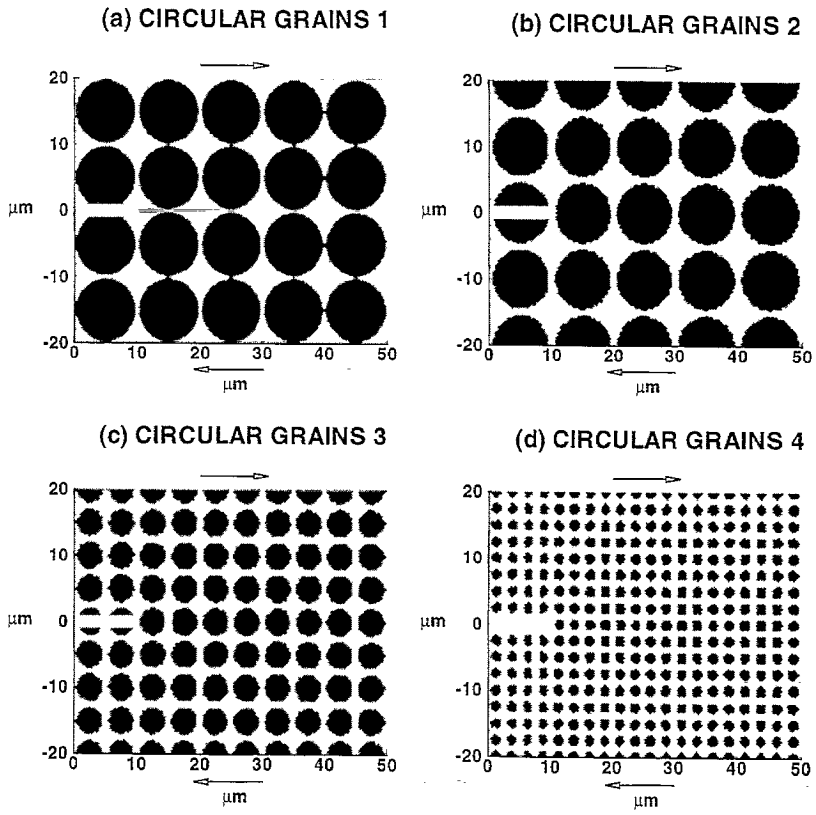

Fig. 2. Microstructures with regular arrays of circular grains used in the analysis: (a) notch located between two rows of grains, grain diameter is 10 μm; (b) notch centered on a row of grains, grain diameter is 10 μm; (c) notch centered on a row of grains, grain diameter is 5 μm; (b) notch centered on a row of grains, grain diameter is 2.5 μm. All four microstructures have the same grain volume fraction of 75.4% and matrix volume fraction of 24.6%.

Fig. 2(b)–(d) allow the effect of grain size on resistance to shear band propagation and shear band path to be analyzed.

V. NUMERICAL RESULTS

In the numerical analysis carried out, the boundary velocity V_0 applied is $10\,\mathrm{ms}^{-1}$. This corresponds to a nominal shear rate of $\dot{\gamma} = V_0/H = 5 \times 10^5\ \mathrm{s}^{-1}$.

V.1. *Propagation of shear bands in microstructure with random phase distribution*

Figure 3 shows the distributions of the equivalent plastic strain rate $\dot{\bar{\epsilon}}$ at 0.2, 0.4 and 0.8 μs after the beginning of deformation. For clear presentation of the data and visualization of the phases, the matrix and the grains are plotted separately. The plots show the progression of deformation. The strain rate in the matrix is higher. The shear band tends to go through the matrix between grains. The strain rate is usually higher for the parts of the grains that are involved in the shear band. Although the shear band follows relatively soft paths which are mostly between grains, it is possible for it to go through the middle of a grain. Note that the shear band is completely inside a grain near the right edge of the materials block, Fig. 3(c). The development of the shear band is at such a rate that by 0.6 μs after the beginning of deformation, the shear band has propagated through the whole ligament. The apparent width of the band is approximately 10 μm. The notch clearly represents the initiation site for the shear band, suggesting potential significance of defects such as microcracks, voids and grain–matrix debonding in promoting shear failure in these materials.

The distributions of temperature at the same times as those in Fig. 3 are shown in Fig. 4. The temperature contours show more smooth variations of temperature between the phases. The width of significant temperature rise, approximately 15 μm, is larger than the width of high strain rate which is approximately 10 μm. At 0.8 μs, the highest temperature inside the shear band is approaches 650 K.

V.2. *Thermal softening in shear bands*

The distributions of the shear component σ_{12} of the Cauchy stress $\boldsymbol{\sigma}$ in the initial Cartesian frame at 0.4, 0.6 and 0.8 μs are shown in Fig. 5. Initially, the stress levels in front of the notch tip are higher, causing the rate of deformation to be higher there. The higher temperatures in this region cause the material to soften progressively. Clearly, this shear stress decreases as the deformation continues in Fig. 6(a)–(c). The reduction in stress seen here is the net decrease caused by thermal softening after rate sensitivity has been taken into account. The stress levels in the matrix are lower than those in the grains. Thermal softening occurs mainly in the grains for the time period shown.

V.3. *Effect of material inhomogeneity*

Figure 6 is a comparison of the distributions of $\dot{\bar{\epsilon}}$ at 0.4 μs for (a) a uniform material with the properties of the matrix phase, (b) a uniform material with the properties of the grains, (c) the microstructure with random phase distribution in Fig. 1, and (d) the microstructure with circular grains in Fig. 2(a). The propagation of shear band is slower

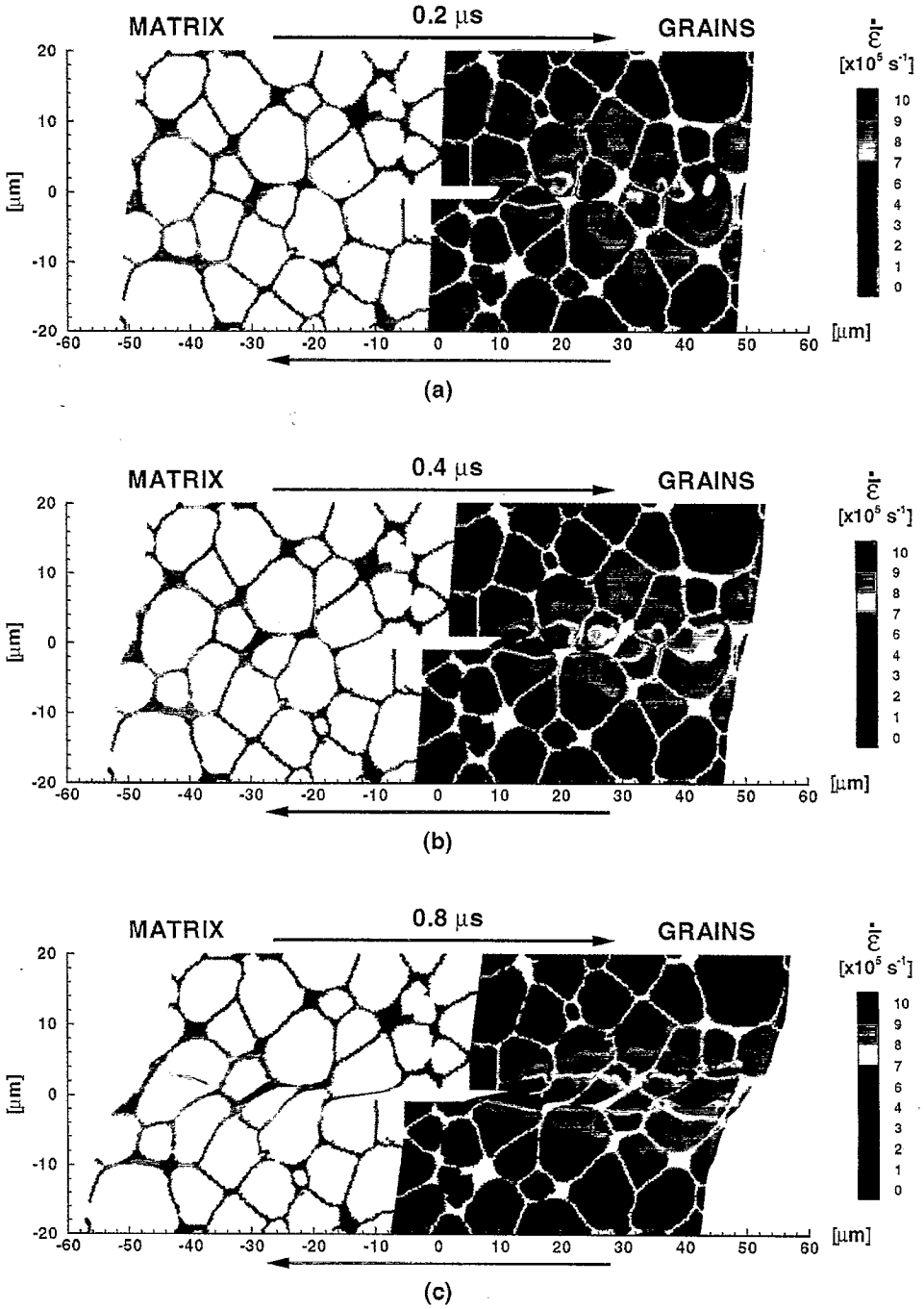

Fig. 3. The distributions of equivalent plastic strain rate at (a) 0.2 μs, (b) 0.4 μs, and (c) 0.8 μs for the microstructure in Fig. 1. The nominal shearing rate is 5×10^5 s^{-1}.

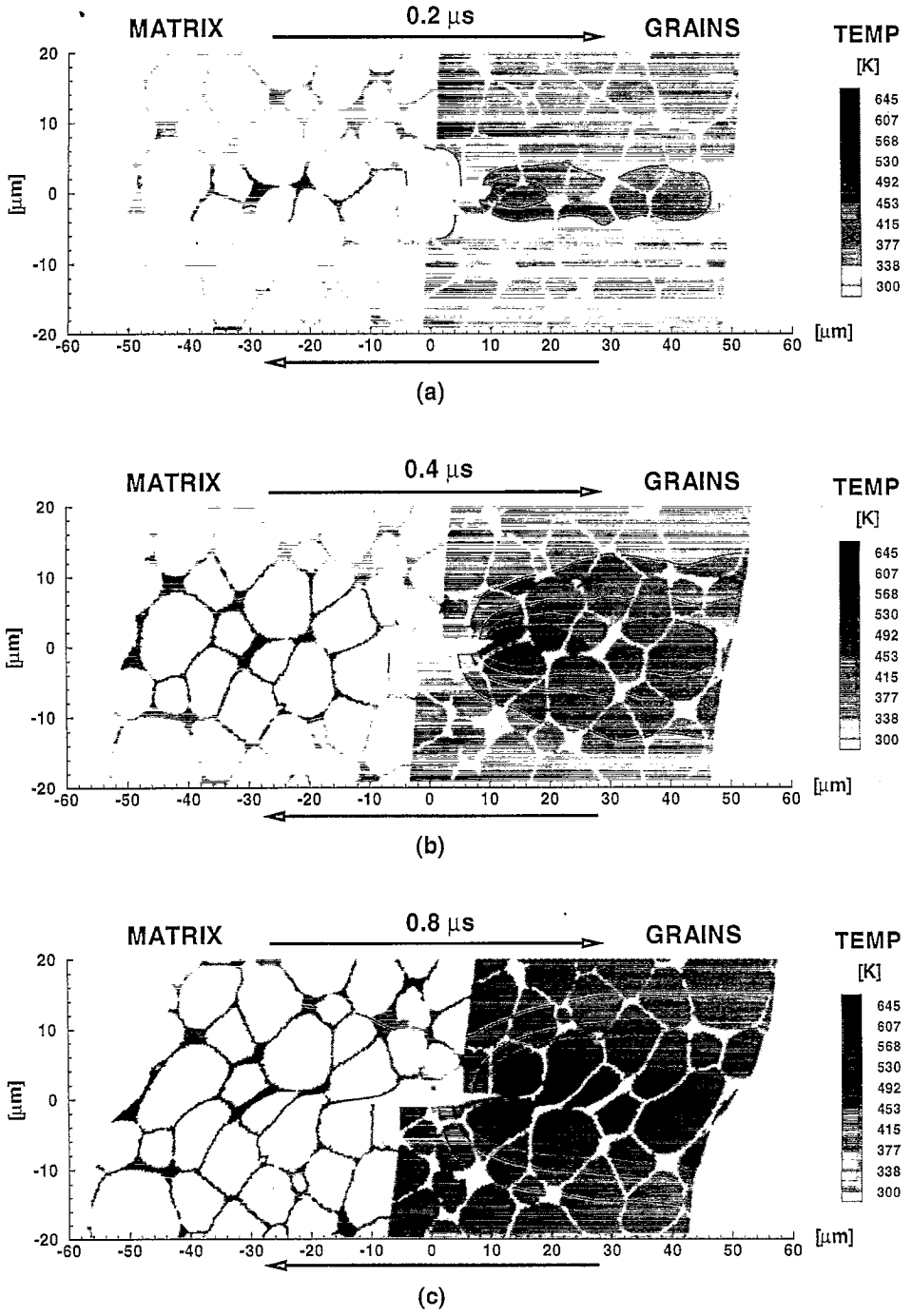

Fig. 4. The distributions of temperature at (a) 0.2 μs, (b) 0.4 μs, and (c) 0.8 μs for the microstructure in Fig. 1. The nominal shearing rate is 5×10^5 s^{-1}.

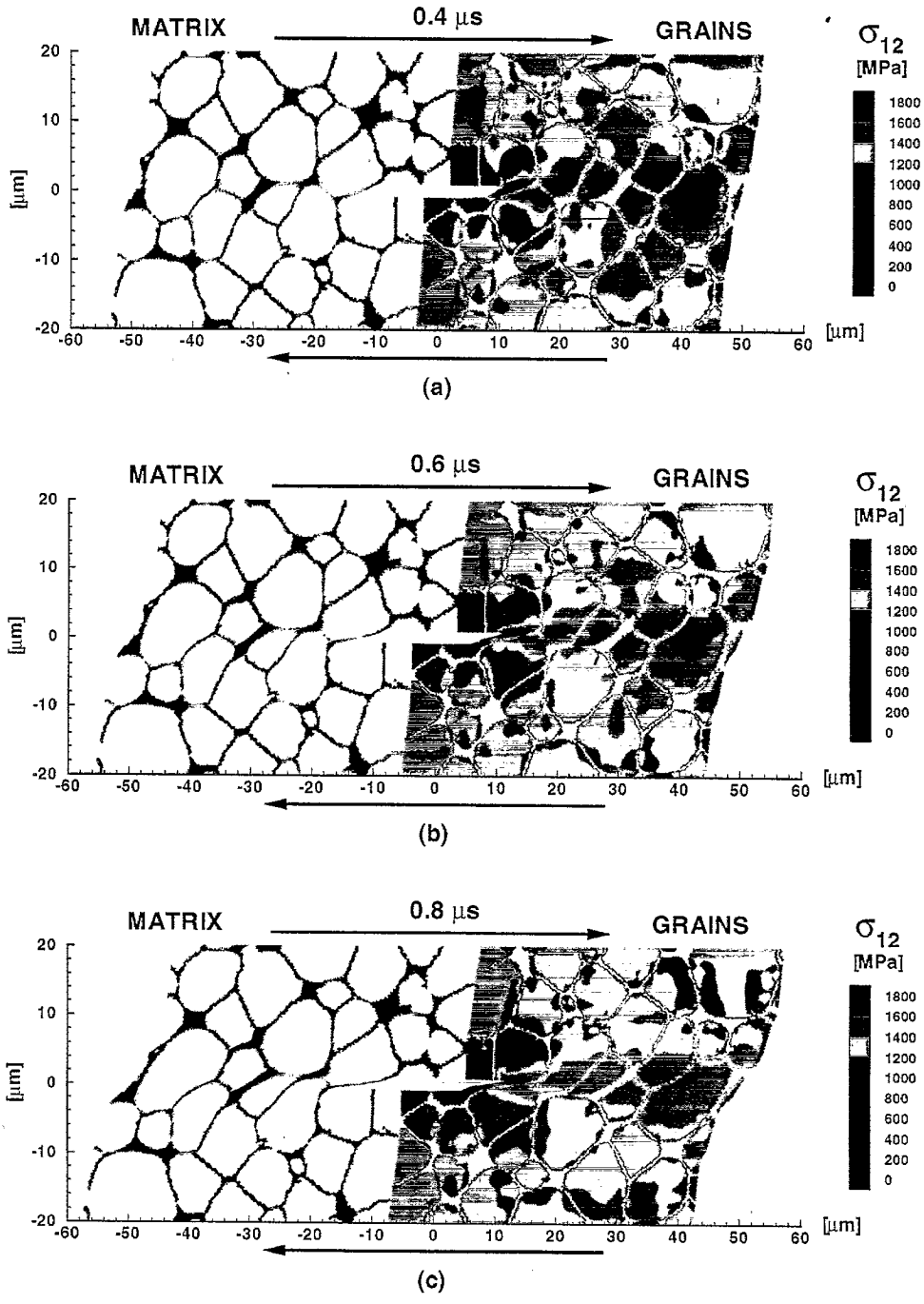

Fig. 5. The distributions of shear stress component σ_{12} at (a) 0.2 μs, (b) 0.4 μs, and (c) 0.8 μs for the microstructure in Fig. 1. The nominal shearing rate is 5×10^5 s^{-1}.

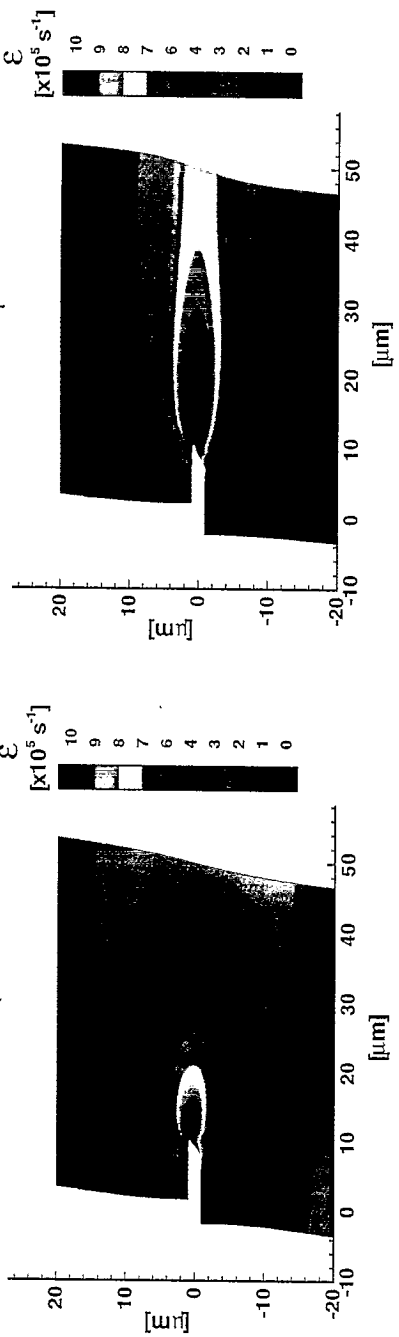

Fig. 6. A comparison of the distributions of equivalent plastic strain rate at 0.4 μs for: (a) a material block with the properties of the matrix material; (b) a material block with the properties of the grain material; (c) the microstructure in Fig. 1; (d) microstructure (a) in Fig. 2.

in the matrix material than that in the grain material. The difference is caused by the fact that the matrix has a higher rate of strain hardening and higher specific heat than the grain material. For the same amount of overall deformation ($t = 0.4 \times 10^{-6}$, $\delta = 0.2$, $\dot{\gamma} = 5 \times 10^5$ s^{-1}), the shear band extension is larger in the grain material, indicating the strong influence of strain hardening and thermal softening on the resistance to shear band propagation. Shear band propagation in the microstructure with random grain–matrix morphology is faster than in either the pure matrix material or in the grain material Fig. 6(c). Clearly, the material inhomogeneities provide an additional driving force for the growth of shear bands, allowing faster propagation. Phase morphology has a direct impact on the growth of shear bands. In Fig. 6(d), the shear deformation is more concentrated in the matrix path between two rows of grains. The propagation of shear band in this microstructure is faster than the propagation in all other cases in Fig. 6. This band forms almost uniformly in the ξ^1 direction, not strongly influenced by the presence of the notch. This indicates that the weakening caused by the regular grain arrangement has a stronger influence on the development of shear bands than the weakening caused by a defect such as the notch. It therefore appears that the reductions in shear failure resistance of the composite materials caused by defects and by phase morphology can both be dominant.

V.4. *Effect of phase morphology*

Figure 7 compares the deformed configurations at 0.8 μs of the four microstructures in Fig. 2. The contours show the distributions of the equivalent plastic strain rate $\dot{\bar{\epsilon}}$. In Fig. 7(a), the location of the notch between two rows of hard grains presents a soft path for the growth of the shear band. Indeed, the shear band forms rather uniformly, almost independently of the notch. The placement of a row of hard grains in front of the notch (Fig. 7(b)) poses a significant impediment to the propagation of the shear band. The grain at the notch tip is severely deformed whereas only nominal deformation is seen for the grains behind it. Two bands of slightly higher rates of deformation are seen above and below this row of grains, indicating the growth of the shear band away from the initial notch line into the relatively soft paths for shear deformation between rows of grains. The dramatically different results in Fig. 7(a) and (b) demonstrate that phase morphology and arrangement can have a significant impact on the propagation of shear bands. Indeed, the distributions of $\dot{\bar{\epsilon}}$ in Fig. 7(a) and (b) show that when the shear band initiation site (the notch) is moved relative to the phases, shear band morphology may undergo significant change. Clearly, hard grains can act as significant obstacles to the development of localization. In this case, the change resulted in the simultaneous development of two shear bands parallel to the direction of shear. The results in Fig. 7(c) and (d) indicate that reducing the size of hard particles makes it easier for shear band to turn into relatively weak regions. The region in front of the notch tip in Fig. 7(c) has two shear bands, one above the notch line and one below the notch line. The shear band in Fig. 7(d) consists of 4–5 subbands of higher rates of deformation. Note that the grain size in Fig. 7(d) of 2.5 μm is significantly smaller than the shear band characteristic width of approximately 10 μm. Therefore, the small grain size makes the material effectively less resistant to shear deformation compared with the microstructure in Fig. 2(b). Instead of concentrating in the matrix as in Fig. 7(a), more deformation is seen in the hard particles. The extent of shear band development in these microstructures can be better seen through the

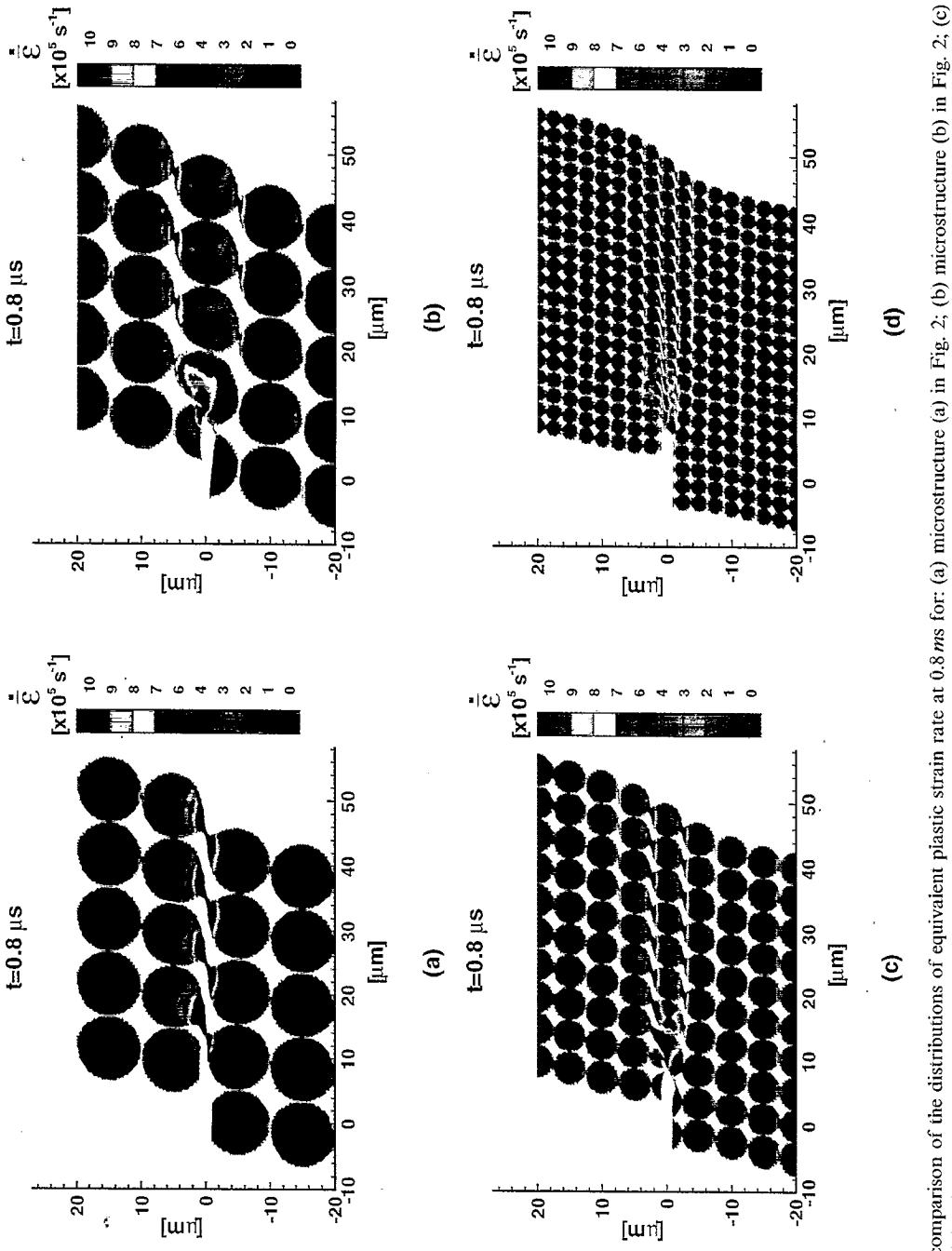

Fig. 7. A comparison of the distributions of equivalent plastic strain rate at 0.8 *ms* for: (a) microstructure (a) in Fig. 2; (b) microstructure (b) in Fig. 2; (c) microstructure (c) in Fig. 2; (d) microstructure (d) in Fig. 2. The nominal shear rate is $5\times10^5\ s^{-1}$.

temperature distributions shown in Fig. 8. The fast localization in Fig. 7(a) corresponds to nominally uniform high temperatures along the direction of shear. The successive reduction of grain size in the microstructures of Figs 2(b)–(d) increases the temperature in front of the notch tip, confirming the softening effect of smaller grains on resistance to shear band propagation seen in Fig. 7.

VI. DISCUSSION

VI.1. *Stress-strain curves*

The nominal shear stress-strain curves for the five composite microstructures and the two monolithic cases (one for the matrix material and one for the grain material) considered are summarized in Fig. 8. The stress shown is the average value of σ_{12} along the lower side of the material block. This stress is used as a measure of the overall stress-carrying capacity of the composite materials in the discussion that follows. The curves for the matrix and the grain materials indicate that the grains have higher strength than the matrix. The curves for the composite microstructures all fall between the curves for the grain material and the matrix material. The formation of shear band has a clear influence on the stress-strain relations. Stress levels for the microstructure in Fig. 1 are higher than those for the other composite microstructures at the same levels of strain. This microstructure has the highest stress-carrying capacity due to its higher grain volume fraction (85% versus 75.4% for the others). However, it poses the least resistance to shear band propagation as indicated by its higher rate of softening as strain increases. This is consistent with what is seen in Figs 4–8. The microstructure in Fig. 2(a) has the lowest stress–strain curve among the composites due to its low resistance to shear band growth. The responses of the microstructures in Fig. 2(b)–(d) are similar to each other, with the smallest grain size producing the weakest overall response. Also, smaller grains seem to cause the stress carried by the materials to decrease more quickly as the shear band develops.

VI.2. *Energy dissipation in phases*

The thermomechanical coupling between the constituent phases directly influences the deformation and the evolution of the load-carrying capacity of the composite materials. Energy evolution in the individual phases provides a perspective on the progression of deformation. The work-energy relation for dynamic deformation is

$$\int_0^t \int_S \mathbf{f}\cdot\dot{\mathbf{u}}\,\mathrm{d}S\mathrm{d}t = \int_0^t \int_V \boldsymbol{\tau} : \mathbf{D}\,\mathrm{d}V\mathrm{d}t + \int_V \frac{1}{2}\rho\dot{\mathbf{u}}\cdot\dot{\mathbf{u}}\,\mathrm{d}V, \tag{17}$$

where $\mathcal{P}(t) = \int_0^t \int_S \mathbf{f}\cdot\dot{\mathbf{u}}\,\mathrm{d}S\mathrm{d}t$ is the accumulated boundary work at time t, $\mathcal{W}(t) = \int_0^t \int_V \boldsymbol{\tau} : \mathbf{D}\,\mathrm{d}V\mathrm{d}t$ is the stress work and the last term in the equation is the kinetic energy stored in the material. This identity specifies the balance between the mechanical work done through the specimen boundary, the stress work and the kinetic energy in the specimen. The stress power consists of an elastic part, a plastic part and a thermal part, i.e.

$$\int_V \boldsymbol{\tau} : \mathbf{D}\,\mathrm{d}V = \int_V \boldsymbol{\tau} : \mathbf{D}^e\,\mathrm{d}V + \int_V \boldsymbol{\tau} : \mathbf{D}^p\,\mathrm{d}V + \int_V \boldsymbol{\tau} : \mathbf{D}^t\,\mathrm{d}V. \tag{18}$$

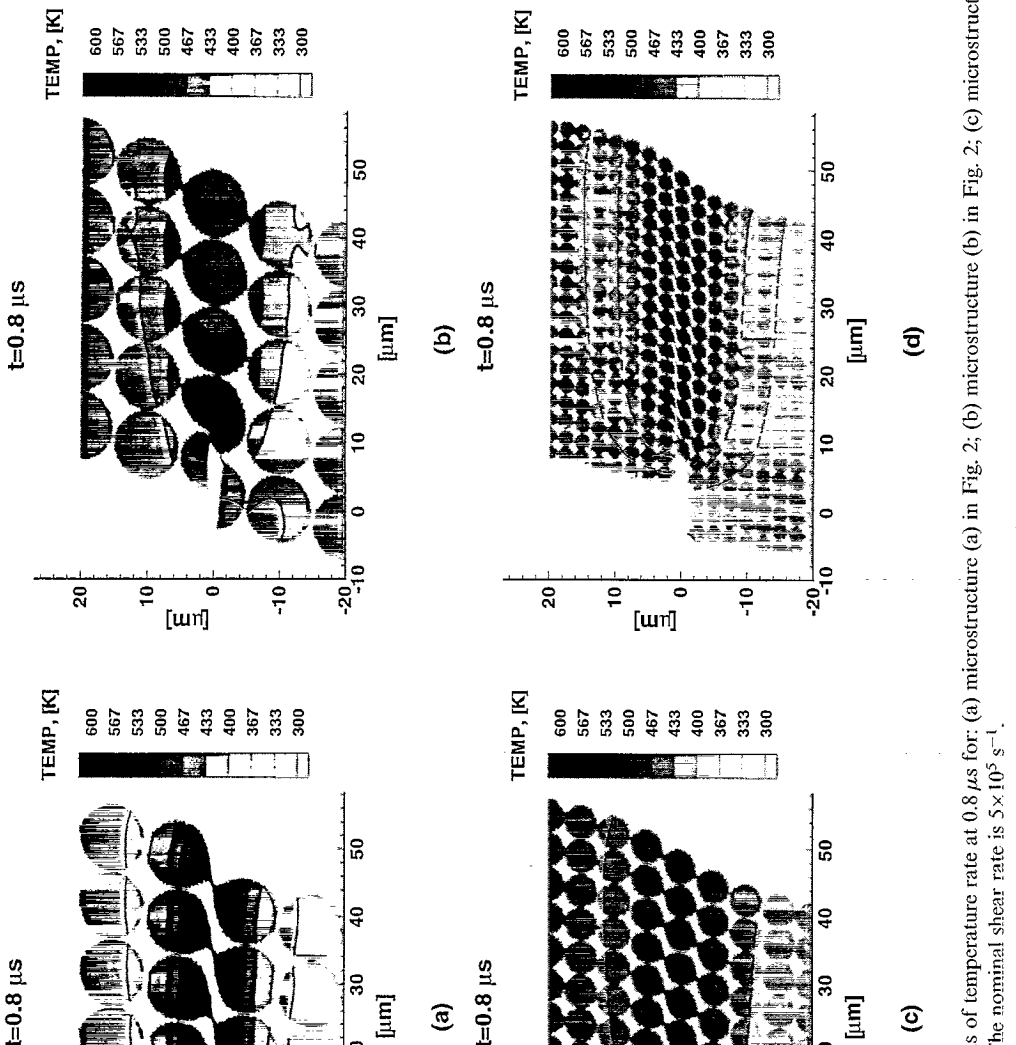

Fig. 8. A comparison of the distributions of temperature rate at 0.8 μs for: (a) microstructure (a) in Fig. 2; (b) microstructure (b) in Fig. 2; (c) microstructure (c) in Fig. 2; (d) microstructure (d) in Fig. 2. The nominal shear rate is $5\times10^5\ s^{-1}$.

These three parts of $\mathcal{W}$ are denoted by $\mathcal{W}^e$, $\mathcal{W}^p$ and $\mathcal{W}^t$, respectively. It is assumed that 90% of the plastic dissipation is converted to heat ($\chi = 0.9$), Taylor *et al.* (1934). The energy balance is governed by the heat equation in the form

$$\int_V \rho c_p \dot{T} \mathrm{d}V = \int_V \chi \boldsymbol{\tau} : \mathbf{D}^p \mathrm{d}V + \int_S k\left(\mathbf{F}^{-1} \cdot \mathbf{F}^{-T} \cdot \frac{\partial T}{\partial x}\right) \cdot \mathbf{n} \mathrm{d}S. \tag{19}$$

The last term is identically zero in the current analysis due to the periodic boundary condition (eqn (12)), the antisymmetric boundary condition (eqn (13)) and the adiabatic boundary condition (eqn (16)). Consequently, no heat is gained or lost for the material blocks considered. Heat exchange occurs only internally within each phase and between the phases. In the discussion that follows, the heat exchange between the two phases are considered. Since calculations have shown that the elastic stress work (or elastic energy stored in the specimen) $\mathcal{W}^e$, the thermal stress work $\mathcal{W}^t$, and the kinetic energy in the specimen remain very small compared with the other terms and are therefore insignificant, only boundary work $\mathcal{P}$, stress work $\mathcal{W}$, and the thermal energy stored in the specimen $\mathcal{E}$ are shown. Except for the boundary work term which represents the amount of mechanical work imparted into the whole specimen, the stress work and thermal energy are measured separately for the grains and the matrix. Specifically, $\mathcal{W}_g = \int_0^t \int_{V_g} \boldsymbol{\tau} : \mathbf{D} \mathrm{d}V \mathrm{d}t$, $\mathcal{W}_m = \int_0^t \int_{V_m} \boldsymbol{\tau} : \mathbf{D} \mathrm{d}V \mathrm{d}t$, $\mathcal{E}_g = \int_{V_g} \rho c_p (T - T_0) \mathrm{d}V$, and $\mathcal{E}_m = \int_{V_m} \rho c_p (T - T_0) \mathrm{d}V$. In the above expressions, V_g and V_m are the volumes of grains and the matrix, respectively. Note that $\mathcal{W}_g \approx \mathcal{W}_g^p$ and $\mathcal{W}_m \approx \mathcal{W}_m^p$, i.e. stress work is mostly spent to cause plastic deformation.

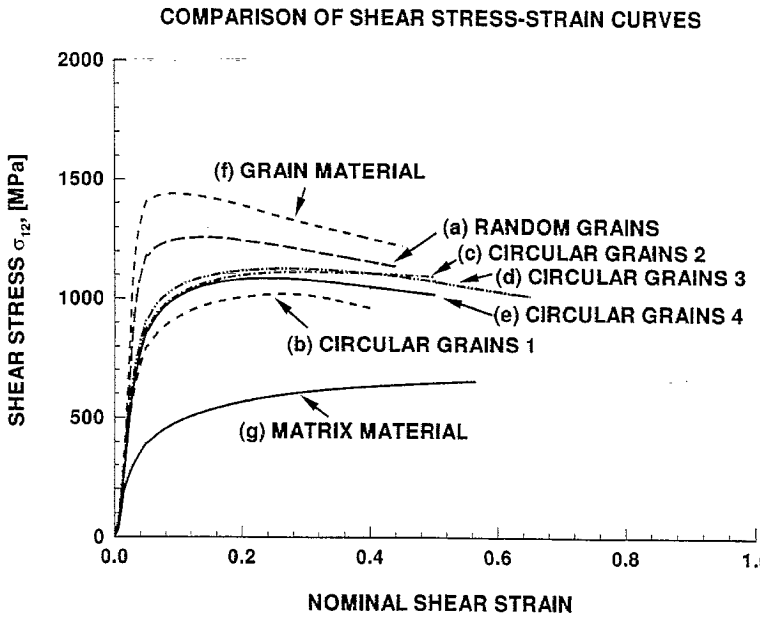

Fig. 9. A comparison of the nominal shear stress–strain curves for the five microstructures in Figs 1 and 2. The curves for two additional calculations are also shown. One uses the uniform properties of the grain material and the other has the properties of the matrix material.

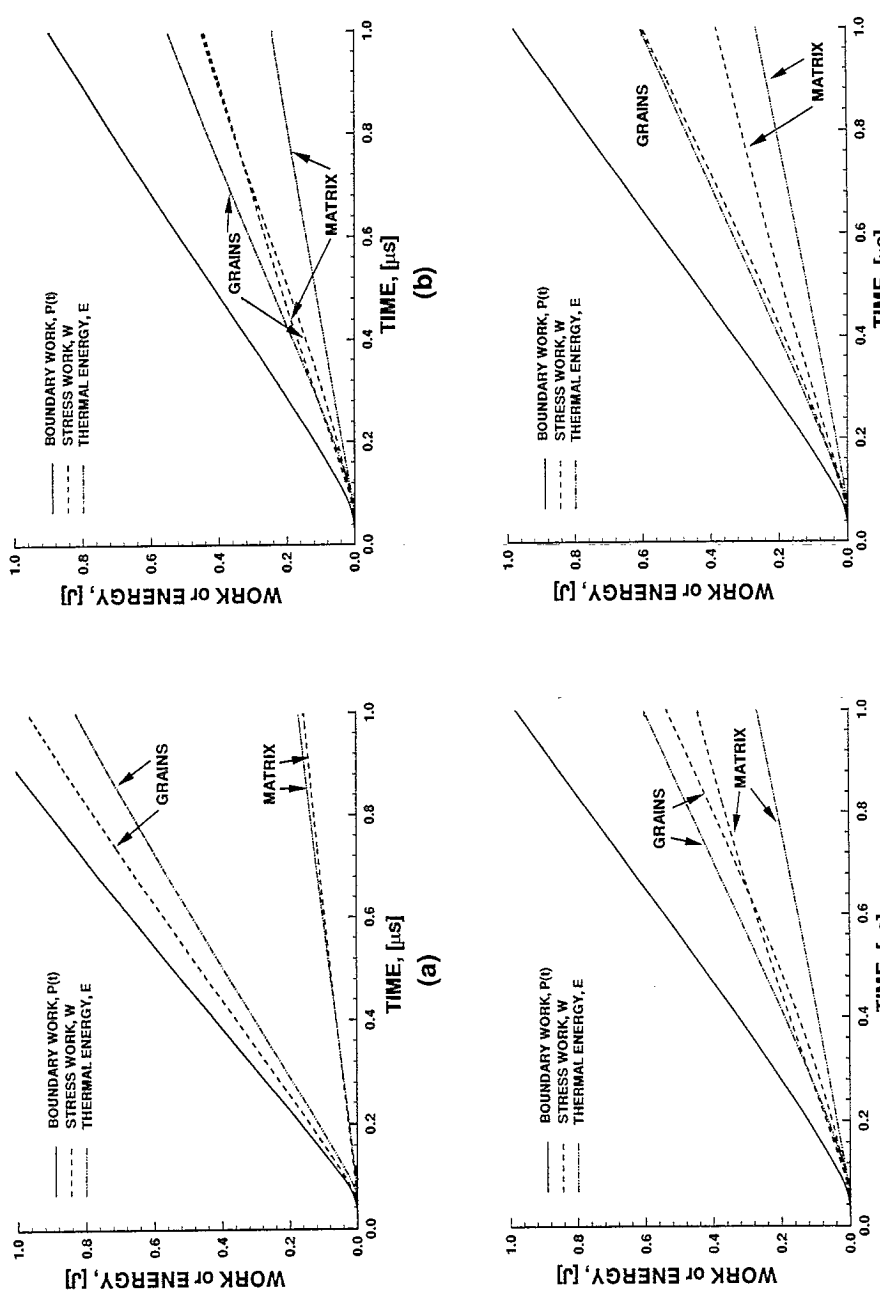

Fig. 10. Evolution of the boundary work $\mathcal{P}(t)$, stress work $\mathcal{W}(t)$ and thermal energy stored $\mathcal{E}(t)$ in the two constituent phases for: (a) the microstructure in Fig. 1; (b) the microstructure in Fig. 2(a); (c) the microstructure in Fig. 2(b); and (d) the microstructure in Fig. 2(c). The nominal shear rate is $5\times10^5\ s^{-1}$.

The histories of these terms for four of the microstructures in Figs 1 and 2 are shown in Fig. 10. The results shown are for (a) the microstructure in Fig. 1, (b) the microstructure in Fig. 2(a), (c) the microstructure in Fig. 2(b), and (d) the microstructure in Fig. 2(c). Under the same nominal shear rate, more mechanical work is required to deform the material block in Fig. 1 than what is required to deform the microstructures in Fig. 2. This is demonstrated in the higher values of boundary work $\mathcal{P}$ in Fig. 10(a) compared with those in Figs 10(b) and (c). This is due to the higher flow stresses resulting from the higher grain volume fraction of this microstructure. For shear bands to grow through the phases, significant fractions of hard grains have to be deformed as well as the softer matrix. Clearly, the random distribution of grain and matrix materials represents a weaker resistance to the development of shear deformation by providing ample opportunities for thermomechanical coupling between the phases. This weaker resistance to deformation is already reflected in the distributions of $\dot{\bar{\epsilon}}$ for this microstructure shown in Fig. 3. It is noted that the matrix phase in this microstructure has more thermal energy stored than the total amount of plastic dissipation generated in it. The extra amount of thermal energy comes from the grains through heat conduction. Clearly, this is a process in which both phases are actively involved in the deformation, contributing to the dissipation of energy.

In contrast, the regular arrangement of grains in the microstructures of Fig. 2(a) causes preferential deformation in the matrix phase by providing readily identifiable soft paths between rows of grains. Since more deformation is concentrated in the matrix, more heat is generated there. Heat conduction allows part of the thermal energy to be diffused into the grains which are at lower temperatures, Fig. 10(b). This flow of heat is the reason why more thermal energy is stored in the grains than what is generated in them. The heat flow into the grains causes additional thermal softening of the grains. Since the volume fraction of the grains is higher than that of the matrix, the fact that comparable amounts of stress work are seen in these phases indicates that the deformation and plastic dissipation occur predominately in the matrix phases. Although changing the relative locations of the notch and the grains has a significant impact on the development and morphology of shear localization, it does not have a significant influence on the work-energy relations in the phases (Figs 10(b) and (c)), suggesting that the inherent partition of dissipation between the phases remains similar. However, this redistribution of deformation does correspond to a significant change in the nominal stress-strain curves Fig. 9.

In Figs 10(c) and (d), the reduction of grain diameter from 10 to 5 μm causes the deformation to shift into the grains. This shift is due to the enhanced heat flow facilitated by the smaller grain diameter. The enhancement in heat exchange and grain softening expedite the growth of shear bands. The redistribution of deformation also causes two or more shear bands to develop. These bands follow soft paths between rows of hard grains. Furthermore, a faster decrease in the stress-carrying capacity is observed; see curves (c) and (d) in Fig. 9.

VII. CONCLUDING REMARKS

The development of shear bands in composite and inhomogeneous materials depends strongly on the thermomechanical coupling between the microscopic phases. The results seen so far demonstrate that phase morphology also has a significant influence. Depending on the needs of specific applications, some phase morphologies may be more desirable

than others. For example, grain arrangement can be used to provide preferential paths and orientations for shear band development. This approach uses the anisotropic response of a composite aggregate. Zhou (1998) analyzed the effects of several microstructural modifications on localization based on a phase morphology similar to that in Fig. 1. The changes considered include addition of a new interfacial layer and the variation of phase properties. Combinations of those changes and appropriate phase arrangement can be used to achieve certain desired performance. For example in structural designs, materials with random phase distributions can be used to obtain materials with weaker resistance to dynamic shear failure. Conversely, ordered phase arrangements can be used to prevent shear localization or to induce it along specific orientations.

The analysis carried out here have considered relatively small samples of material microstructures. Consequently, periodic boundary conditions have been used to reduce the size of the numerical model. The size scale effect on localization in such materials have not been fully analyzed. More realistic treatment of the problems requires substantially more powerful computational resource than the Cray C90 computer used in this study. Furthermore, extension to a three-dimensional framework of analysis as part of future investigations may also yield new insight into the problems and render more realistic consideration of microscopic inhomogeneities.

Acknowledgements—Support from the Office of Naval Research through grant no. N00014-96-1195 to Georgia Tech is gratefully acknowledged. The calculations were carried out on Cray supercomputers at the Jet Propulsion Laboratory, the Goddard Space Center and the SDSC.

REFERENCES

Andrews, E. W., Bower, A. F. and Duffy, J. (1992) Shear band formation in a tungsten heavy alloy. Proc. Symposium on Shear Bands and Viscoplastic Theories, The 29th Annual Technical Meeting of the Soc. for Engng. Sci., 14–16 September, La Jolla, CA.

Belytschko, T., Chiapetta, R. L. and Bartel, H. D. (1976) Efficient large scale non-linear transient analysis by finite elements. *Int. J. Numer. Meth. Engng.* **10**, 579–596.

Krieg, R. D. and Key, S. W. (1973) Transient shell response by numerical time integration. *Int. J. Numer. Meth. Engng.* **7**, 273–286.

Lankford, J., Bose, A., Couque, H. and Anderson, C. E., (1991) The role and microstructure in the deformation and failure of tungsten heavy alloys. *Proc. 12th Army Symposium on Solid Mechanics*, Plymouth, MA, pp. 117–138.

Lemonds, J. and Needleman, A. (1986) Finite element analyses of shear localization in rate and temperature dependent solids. *Mech. Mater.* **5**, 339–361.

Magness, L. S. (1994) High strain rate behaviors of kinetic energy penetrator materials during ballistic impact. *Mech. Mat.* **17**(2–3), 147–154.

Needleman, A. (1989) Dynamic shear band development in plane strain. *J. Appl. Mech.* **56**, 1–9.

Needleman, A. and Tvergaard, V. (1991) An analysis of dynamic, ductile crack growth in a double edge cracked specimen. *Int. J. Frac.* **49**, 41–67.

Peirce, D., Shih, C. F. and Needleman, A. (1984) A tangent modulus method for rate dependent solids. *Comp. Struct.* **18**, 875–887.

Taylor, G. I. and Quinney, H. (1934) The latent energy remaining in a metal after cold working. *Proc. R. Soc.* **A143**, 307–326.

Weerasooriya, T., Beaulieu, P. A. and Swanson, R., (1992) Deformation and failure behavior of 93W–5Ni–2Fe at high strain rate shear loading. U.S. Army Materials Technology Laboratory Report, no. MTL TR 92–19, Watertown, MA.

Yadav, S. and Ramesh, K. T. (1995) The mechanical properties of tungsten-based composites at very high strain rates. *Mater. Sci. Engng.* **A203**, 140–153.

Zhou, M., (1998) Effects of microstructure on resistance to shear localization for a class of metal matrix composites. *Fatigue Fract. Engng. Mat. Struct.*, **21**(4), 425–438.

Zhou, M. and Clifton, R. J., (1997) Dynamic constitutive and failure behavior of a two-phase tungsten composite. *J. Appl. Mech.*, **64**, 487–494.

Zhou, M., Clifton, R. J. and Needleman, A. (1992) Shear band formation in a W–Ni–Fe alloy under plate impact. *Proc. Int. Conf. on Tungsten and Tungsten Alloys*, November, Arlington, VA, pp. 343–356.

Zhou, M., Needleman, A. and Clifton, R. J. (1994) Finite element simulations of dynamic shear localization. *J. Mech. Phy. Solids* **42**(3), 423–458.